

GT2011-45190

**SIMULATIONS OF MULTI-PHASE PARTICLE DEPOSITION ON  
ENDWALL FILM-COOLING HOLES IN TRANSVERSE TRENCHES**

**Seth A. Lawson and Karen A. Thole**  
The Pennsylvania State University  
Department of Mechanical and Nuclear Engineering  
University Park, PA, USA

**ABSTRACT**

Integrated gasification combined cycle (IGCC) power plants allow for increased efficiency and reduced emissions as compared to pulverized coal plants. A concern with IGCCs is that impurities in the fuel from the gasification of coal can deposit on turbine components reducing the performance of sophisticated film-cooling geometries. Studies have shown that recessing a row of film-cooling holes in a transverse trench can improve cooling performance; however, the question remains as to whether or not these improvements exist in severe environments such as when particle deposition occurs.

Dynamic simulations of deposition were completed using wax injection in a large-scale vane cascade with endwall film-cooling. Endwall cooling effectiveness was quantified in two specific endwall locations using trenches with depths of 0.4D, 0.8D, and 1.2D, where D is the diameter of a film-cooling hole. The effects of trench depth, momentum flux ratio, and particle phase on adiabatic effectiveness were quantified using infrared thermography. Results showed that the 0.8D trench outperformed other geometries with and without deposition on the surface. Deposition of particles reduced the cooling effectiveness by as much as 15% at  $I = 0.23$  with the trenched holes as compared to 30% for holes that were not placed in a transverse trench.

**NOMENCLATURE**

a speed of sound  
A surface area  
C chord length  
 $C_p$  particle specific heat  
 $\Delta h_{fus}$  specific latent heat of fusion  
D film cooling hole diameter,  $D=0.46\text{cm}$   
 $d_p$  particle diameter  
h trench depth  
I momentum flux ratio,  $I = \rho_c U_c^2 / \rho_\infty U_\infty^2$   
L film cooling hole length  
 $L_c$  characteristic length for Stokes number  
 $L_p$  particle travel distance

M film cooling blowing ratio,  $M = \rho_c U_c / \rho_\infty U_\infty$   
 $M_{ideal}$  ideal blowing ratio,  $M_{ideal} = \sqrt{\rho_c (P_{c,\infty} - P_\infty) / \rho_\infty (P_{o,\infty} - P_\infty)}$   
Ma Mach number,  $Ma = U_\infty / a$   
p static pressure  
P vane cascade pitch  
 $P_o$  total pressure  
Q heat loss to surroundings  
Re Reynolds number,  $Re = \rho U_\infty C / \mu$   
S nozzle guide vane span  
Stk Stokes number,  $Stk = \rho_p d_p^2 U_p / 18 \mu L_c$   
T temperature  
 $t_1$  time for particle to reach  $T_{p,s}$ ,  $t_1 = -\frac{\rho_p C_p V_p}{h A_p} \ln \left[ \frac{T_{p,s} - T_\infty}{T_{p,i} - T_\infty} \right]$   
 $t_2$  time for particle to release  $\Delta h_{fus}$ ,  $t_2 = \frac{\Delta h_{fus} \rho_p V_p}{h A_p (T_{p,s} - T_\infty)}$   
TSP thermal scaling parameter,  $TSP = (t_1 + t_2) / (L_p / U_\infty)$   
Tu turbulence intensity percent,  $Tu = u_{rms} / U_\infty$   
U velocity  
V volume  
X,Y,Z local coordinates  
**Greek**  
 $\eta$  adiabatic effectiveness,  $\eta = (T_\infty - T_{aw}) / (T_\infty - T_c)$   
 $\bar{\eta}$  laterally-averaged effectiveness  
 $\bar{\bar{\eta}}$  area-averaged effectiveness  
 $\bar{\bar{\eta}}_0$  baseline area-averaged effectiveness (no deposition)  
 $\rho$  density  
 $\mu$  gas dynamic viscosity  
**Subscripts**  
aw adiabatic wall  
c coolant  
ex exit  
i initial  
in inlet

p particle  
s solidification  
 $\infty$  inlet mainstream

## INTRODUCTION

Improvements in turbine design in the last half century have allowed for increased turbine inlet temperatures and improved gas turbine performance. Because exhaust gases exceed melting temperatures of downstream turbine components, cooling methods, such as film-cooling, are required to prevent turbine component failure due to thermal fatigue. An added element to the already complicated problem of turbine cooling is that impurities in the air and fuel can deposit on turbine components impairing aerodynamic performance and reducing film-cooling benefits. The physical problem is the same in aircraft engines and land based gas turbines; however, many factors including the melting temperatures of the impurities as well as the combustion temperature of the engine can differ and play a significant role in the extent of damage caused by particle deposition. In IGCC power plants, particle impurities as large as  $10\mu\text{m}$  that exist in the syngas can reach high enough temperatures in the combustor to become sticky and deposit on downstream turbine components. Simulated deposition studies have shown that deposition in and around film-cooling holes can reduce cooling effectiveness by as much as 30% on the endwall [1].

Improvements in cooling performance can be achieved by embedding a film-cooling row of holes into a transverse trench allowing for increased coolant flow without the risk of jet separation [2, 3]. Studies have shown that trench cooling may mitigate the negative effects of deposition on film-cooling performance [3, 4]; however, the impact of dynamically simulated deposition on trenched film-cooling effectiveness has never been quantified.

For the current study, a method previously described by Lawson and Thole [1] was used to dynamically simulate particle deposition using wax to determine the effects of deposition on the performance of film-cooling holes in a transverse trench. Endwall film-cooling rows near the vane leading edge were embedded in trenches with depths of  $0.4D$ ,  $0.8D$ , and  $1.2D$ . Deposition was simulated for three momentum flux ratios at all three trench depths. The  $0.8D$  trench was used to determine the effects of particle phase on deposition and the resulting cooling effectiveness.

## REVIEW OF RELEVANT LITERATURE

The concept of embedding coolant holes in a transverse trench was introduced as a method that could be easily manufactured with a slight modification to the thermal barrier coating process [5]. Waye and Bogard [6] measured adiabatic effectiveness for a row of cooling holes in various trench configurations on the suction side of a turbine vane. They found that the ideal geometry had the downstream edge of the trenched cooling row located at the hole exit. This ideal geometry resulted in increased lateral spreading of the coolant and improved adiabatic effectiveness by up to 100% at the hole trailing edge and up to 40% downstream. Sundaram and Thole [3] and Harrison et al. [2] concluded that the trench allowed for

increased coolant flow without the increased risk of jet separation at high blowing ratios.

Studies by Somawardhana and Bogard [4], and Sundaram and Thole [3] showed promise that the trench could reduce the negative impact of deposition on cooling effectiveness. Deposition using idealized roughness elements indicated that the transverse trench improved cooling effectiveness and eliminated the negative effects of roughness and deposition [4]. Sundaram and Thole [3] observed no major effect on cooling performance when bumps with heights of  $0.5D$  and  $0.8D$  were placed downstream of cooling holes; however, the bump with a height of  $1.2D$  enhanced effectiveness by approximately 20%.

In contrast to the methods used by Somawardhana and Bogard [4] and Sundaram and Thole [3] in which deposition was simulated using idealized elements, deposition has also been simulated dynamically by various researchers. Jensen et al. [7] used the Turbine Accelerated Deposition Facility (TADF) to simulate 10,000 hours of turbine operation in a four hour test by increasing the concentration of particulate matter in the hot gas path. Smith et al. [8] used a similar accelerated technique to simulate deposition in a true scale nozzle guide vane cascade using the Turbine Reacting Flow Rig (TuRFR). They found that mainstream temperature and film-cooling operating conditions have a significant effect on deposition, observing that surface deposition increased significantly with an increase in mainstream temperature. This finding supports the results in the literature that show deposition is highly dependent on the relationship between particle melting temperature and mainstream gas temperature [9-12].

The method developed by Jensen et al. [7] was later used by Ai et al. [13] who used the TADF to observe deposition and its effects on trenched film-cooling holes at various impingement angles. Without deposition, the trench improved cooling at shallow impingement angles; however, during deposition simulation, particles accumulated inside the downstream lip of the trench leading to hole blockage and reduced cooling.

Lawson and Thole [1, 14] and Albert et al. [15] dynamically simulated deposition using wax in facilities operating at near standard temperature and pressure conditions. Wax was used to simulate both molten and solid particles in all three studies to observe deposition and its effect on film-cooling.

Lawson and Thole [14] simulated deposition using wax in the vicinity of a row of film-cooling holes on a flat plate and quantified the effects of deposition on cooling effectiveness at three momentum flux ratios. Results showed that deposition reduced cooling effectiveness by as much as 25% at low momentum flux ratios. They determined that the effect of deposition on effectiveness reached an equilibrium state at which point further deposition on the surface had little-to-no effect on cooling effectiveness.

Albert et al. [15] simulated deposition on a vane leading edge with showerhead film cooling. They determined that deposition built up on the surface and reached a quasi-steady state. They also determined that blowing ratio as well as the relationship between wax solidification temperature and the mainstream gas temperature had a significant effect on deposition formation.

The wax simulation method was further developed by Lawson and Thole [1] who verified that deposition reached an equilibrium state as predicted by Lawson and Thole [14] and Albert et al. [15]. A Thermal Scaling Parameter (TSP), which scaled the solidification time of the particles from engine to laboratory conditions, was developed by Lawson and Thole [1]. They quantified the effects of TSP and momentum flux ratio on film-cooling effectiveness and determined that deposition reduced effectiveness by as much as 30% depending on cooling row location, TSP, and momentum flux ratio.

For the current study, the wax deposition method developed by Lawson and Thole [1] was used to determine the effects of dynamically simulated deposition on the effectiveness of cooling rows embedded in transverse trenches. The vane cascade and trenched cooling geometries used in the current study are similar to those used by Sundaram and Thole [3]. In addition to the cooling row at the vane endwall junction studied by Sundaram and Thole [3], a passage cooling row and a pressure side row were embedded into transverse trenches with depths of  $0.4D$ ,  $0.8D$ , and  $1.2D$ . Past research has shown that deposition can have a negative effect on typical film-cooling geometries; however, evidence outlined in this review of literature suggests that trenched film-cooling geometries can improve cooling effectiveness and possibly mitigate the negative effects of deposition.

## EXPERIMENTAL METHODS

Experiments were conducted in a low speed closed loop wind tunnel. Flow through the facility, shown in Figure 1, was powered by a 37 kW axial fan. After passing through a primary heat exchanger, the flow split into a mainstream flow path and two secondary cooling flow paths. Secondary heat exchangers were used to maintain the coolant temperature at 298K while a heater bank was used to achieve mainstream gas temperatures as high as 338K. The heated mainstream flow passed through flow conditioning screens and honeycomb to straighten the flow and ensure uniformity across the channel. A turbulence grid which generated 4% turbulence intensity with a length scale of  $4.4D$  at the vane leading edge [16] was located  $3.6C$  upstream of the large scale vane cascade.

The vane geometry and operating conditions used in this study are shown in Table 1 and described in detail by Radomsky and Thole [17]. The 9X scale cascade consisted of two full passages with one full vane and two neighboring half vanes. The endwall film-cooling geometry is illustrated in Figure 2. A  $45^\circ$  angled slot located upstream of the cascade was present to simulate coolant leakage at the interface between the combustor and the turbine. It is important to note that the leakage coolant to mainstream mass flux ratio was 0.75% for every experiment conducted in the study. The endwall was constructed out of low thermal conductivity polyurethane foam ( $k = 0.033$  W/m-K). A balsawood ( $k = 0.055$  W/m-K) layer, as shown in Figure 2, was added on top of the foam in the leading edge region to build up the necessary thickness for each trench geometry tested. Adiabatic effectiveness was quantified on the leading edge region of the endwall for cooling rows with trench depths of  $0.4D$ ,  $0.8D$ , and  $1.2D$ . Figure 2b shows that the leading edge cooling row was aligned with the flow, and the passage cooling row was oriented at a compound angle of  $90^\circ$

relative to the flow. All film-cooling holes were drilled at  $30^\circ$  inclined angles and the coolant flow direction for each row is indicated by the arrows in Figure 2b. For the leading edge cooling row, the trench was  $25D$  long and  $2D$  wide and for the passage cooling row the trench was  $22D$  long and  $1D$  wide. A variable speed blower was used to supply coolant from the upper secondary flow path to two separate coolant plenums located under the test section. One coolant plenum supplied coolant to the upstream slot while another plenum supplied coolant to the endwall film-cooling holes. Film-cooling flow conditions were characterized by the momentum flux ratio

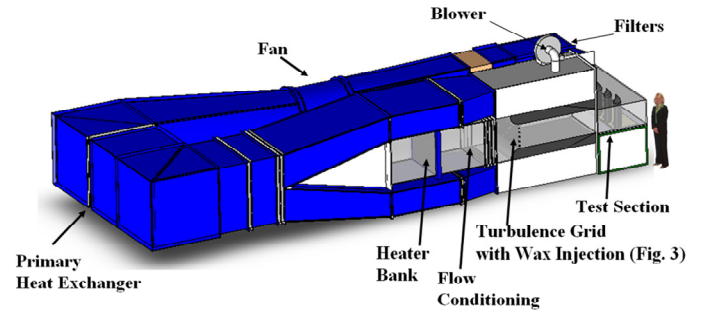


Figure 1. Illustration of wind tunnel facility.

Table 1. Geometric and Flow Conditions

Scaling factor	9
Scaled up chord length, $C$	59.4 cm
Pitch/Chord, $P/C$	0.7
Span/Chord, $S/C$	0.93
Hole, $L/D$	8.3
$Re_{in}$	$2.25 \times 10^5$
Inlet and exit angles	$0^\circ$ and $72^\circ$
Inlet, exit Mach number, $Ma_{in}$ , $Ma_{ex}$	0.012, 0.085
Inlet mainstream velocity, $U_\infty$	6.3 m/s

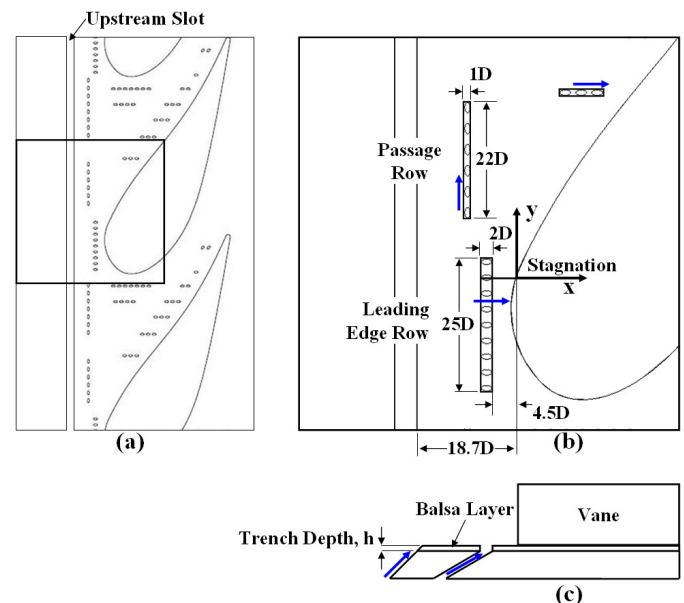


Figure 2. Schematic of the (a) endwall film cooling configuration, (b) leading edge region, and (c) cross-section of the stagnation region.

derived from the ideal blowing ratio,  $M_{ideal}$ , of the leading edge cooling hole located directly upstream of the stagnation point. Experiments were conducted at momentum flux ratios of 0.23, 0.95, and 3.6 to characterize a wide range of operating conditions. The ideal blowing ratios for the three cooling conditions tested were 0.5, 1.0, and 2.0.

### **Adiabatic Effectiveness Measurements**

Steady state experiments were conducted to measure spatially-resolved adiabatic wall temperatures using infrared (IR) thermography. A FLIR SC620 IR camera was used to measure adiabatic wall temperatures with 0.08D resolution.

Experiments were conducted for approximately four hours to reach steady state at which point five IR photographs were taken of the endwall at five locations around the leading edge region. Each image was calibrated using thermocouples mounted in discrete locations on the endwall. Calibrations were performed by adjusting the surface emissivity and background temperature until IR image data matched thermocouple data from corresponding locations in each image. At least two thermocouples were used to calibrate each IR image. After calibrating every acquired image, the five images at each location were averaged to attain one data set for each image location. The five data sets were then joined together to form a composite temperature map of the entire leading edge region. The endwall temperature map for each case was then used to generate a contour of adiabatic effectiveness levels. A correction described in detail by Lawson and Thole [1] was used to account for 1-D conduction losses through the endwall into the coolant plenum.

### **Uncertainty Analysis**

The uncertainty analysis conducted using the propagation method by Moffat [18] showed that momentum flux ratio uncertainty was  $\pm 0.0285$  (3.0% at  $I=0.95$ ). The bias and precision uncertainties for thermocouples used for measuring gas temperatures were  $0.5^\circ\text{C}$  and  $0.12^\circ\text{C}$  respectively. The IR temperature data after calibration yielded bias and precision uncertainties of  $0.51^\circ\text{C}$  and  $0.34^\circ\text{C}$  respectively. Resulting uncertainties in adiabatic effectiveness were  $\pm 0.028$  at  $\eta = 0.14$  and  $\pm 0.021$  at  $\eta = 0.89$ .

### **Dynamic Deposition Simulation and Analysis**

A two-nozzle particle generator was used to inject wax particles into the mainstream flow. The development of the deposition method used in this study was described in detail by Lawson and Thole [1]. The wax injection nozzles were installed in the turbulence grid, as shown in Figure 3, to minimize any flow obstruction caused by the system. Control over particle size distribution was achieved with independent control over liquid wax pressure and atomizing air pressure.

The Stokes number and Thermal Scaling Parameter (TSP) were used to scale particle trajectories and particle phase respectively. The Stokes number is a non-dimensional particle response time and has been used in the literature [19] to scale particle inertial behavior in turbine cascades. Lawson and Thole [1] developed the TSP to scale the phase change process

of the particles in the mainstream. The deposition probability of a given particle is highly dependent on the phase of the particle upon impaction of the surface. Described in detail by Lawson and Thole [1], the TSP is the solidification time of a particle immersed in a gas of a lower temperature and scaled using the time it takes the particle to travel from the combustor to the surface of interest. Particles with TSP values less than one are in solid form upon reaching the vane cascade while particles with TSP values greater than one are in molten form. Because TSP is highly dependent on particle size, the TSP of the maximum particle size generated ( $100\mu\text{m}$ ) is used to characterize each experiment. The equations used for calculating TSP are shown in the nomenclature.

An analysis performed by Lawson and Thole [1] revealed that wax particles between 1 and  $100\mu\text{m}$  would match the Stokes numbers of fly ash particles between  $0.1$  and  $10\mu\text{m}$  that exist in a gas turbine. To generate particles between 1 and  $100\mu\text{m}$ , the appropriate liquid wax pressure and atomizing air pressure were used for the system shown in Figure 3. A separate analysis was performed by Lawson and Thole [1] to determine that the TSP value of a  $10\mu\text{m}$  fly ash particle in an engine is 1.2. For the current study, experiments were conducted at  $TSP_{max}$  values of 1.2 and 2.2 to determine the effects of particle phase on deposition and the resulting cooling effectiveness. To achieve  $TSP_{max} = 1.2$ , wax with a solidification temperature of 351 K was injected into the mainstream gas path at  $T_\infty = 337\text{K}$ . Wax with a solidification temperature of 333 K was injected into the mainstream gas path at  $T_\infty = 325\text{K}$  to achieve  $TSP_{max} = 2.2$ . Table 2 shows the particle properties and scaling parameters for the deposition simulations conducted for the current study. It is important to note that liquid wax and atomizing air pressures were set accordingly to achieve the same particle size distribution with both types of waxes used.

Lawson and Thole [1] conducted experiments with varying amounts of wax and determined that deposition reached an equilibrium state after 900 g of wax injection. They determined that the effects of deposition on cooling effectiveness had reached an equilibrium state when additional injection of wax no longer reduced cooling effectiveness. Between 600g and 900g of wax injection, effectiveness reduction, caused by deposition, changed by only 1%. For the current study, wax particles were injected into the mainstream at a rate of 3.8 g/s for approximately 240 s amounting to a total

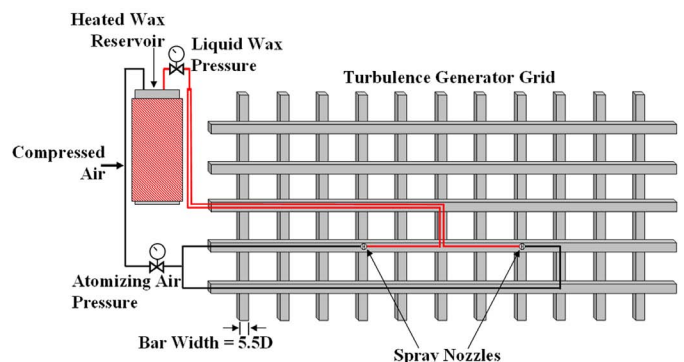


**Figure 3. Schematic of turbulence grid with wax injection system developed by Lawson and Thole [1].**

**Table 2. Particle Properties and Scaling Parameters**

	Engine (Fly Ash)	Laboratory (Wax1/Wax2)
Particle Diameter, $d_p$ ( $\mu\text{m}$ )	0.1 - 10	1 - 100
Particle Density, $\rho_p$ ( $\text{kg/m}^3$ )	1980 [20]	800
Specific Latent Heat of Fusion, $\Delta h_{\text{fus}}$ (J/kg)	650000 [21]	225600
Specific Heat, $C_p$ (J/kg-K)	730 [22]	2090
Particle Softening Temperature, $T_{p,s}$ (K)	1533 [23]	351/333
Mainstream Gas Temperature, $T_\infty$ (K)	1500 [24]	337/325
Particle Initial Temperature, $T_i$ (K)	1593 [24]	364
Gas Viscosity, $\mu$ ( $\text{kg/m-s}$ )	$5.55 \times 10^{-5}$	$1.82 \times 10^{-5}$
Particle Travel Distance, $L_\infty$ (m)	0.26	2.34
Particle Velocity (Mainstream Velocity), $U_\infty$ (m/s)	93 [25]	6.3
Film Cooling Hole Diameter, $D$ (mm)	0.5	4.6
Maximum Thermal Scaling Parameter, $\text{TSP}_{\text{max}}$	1.2	1.2/2.2
Stokes number, $\text{Stk}$	0.004 - 40	0.004 - 40

of 900 g of wax injection for each deposition simulation. After completing the deposition simulation, the surface was photographed as detailed by Lawson and Thole [1]. A thin layer of flat black paint was then applied to the deposition laden surface to ensure that the emissivity was uniform and close to one across the surface to ensure accurate IR thermography measurements.

### Flow Visualization Methods

Flow visualization experiments were conducted using high speed images of wax particles immersed in the flowfield. A 2000 Hz CMOS camera with 1024 x 1024 pixel resolution was used to capture images while a Nd:YLF pulsed laser was used as a light source. The laser pulse frequency used for these experiments was approximately 6000 Hz. By pulsing the laser at three times the rate of the camera speed, multiple exposed images were acquired for improved flow visualization. The laser was mounted on top of the test section and was used to illuminate the stagnation plane indicated in Figure 2b. To capture images of particles passing through the stagnation plane, the camera was placed approximately  $10^\circ$  from normal to the stagnation plane at a distance of approximately 0.6 m. Successive images were then summed together to create composite images that illustrate particle trajectories of individual particles as they interact with secondary flow structures in the stagnation plane.

### DISCUSSION OF RESULTS

The following section discusses the effects of trench depth, momentum flux ratio, and thermal scaling parameter on deposition and the resulting cooling effectiveness in the leading edge region. The effects of trench depth without deposition are discussed first followed by a discussion of the effects of trench depth, momentum flux ratio and thermal scaling parameter on cooling with deposition.

#### Effects of Trench Depth with No Deposition

By embedding the film-cooling holes into a transverse trench, the tendency of a jet to separate from the surface is reduced. The trench effectively channels the coolant along the length of the trench improving cooling within the trench as well as downstream of the trench. Sundaram and Thole [3] concluded that the effectiveness of the trench is sensitive to its

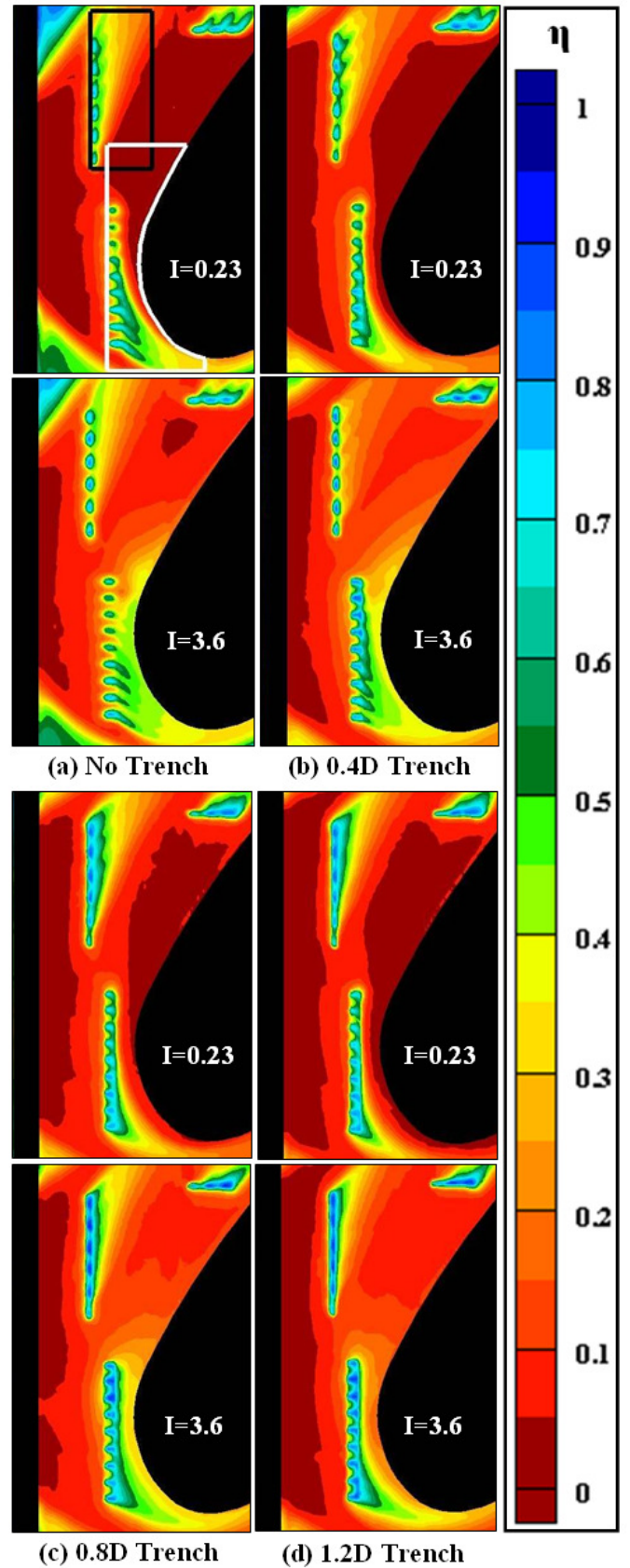


**Figure 4. Contours of adiabatic effectiveness for different trench depths with no deposition.**

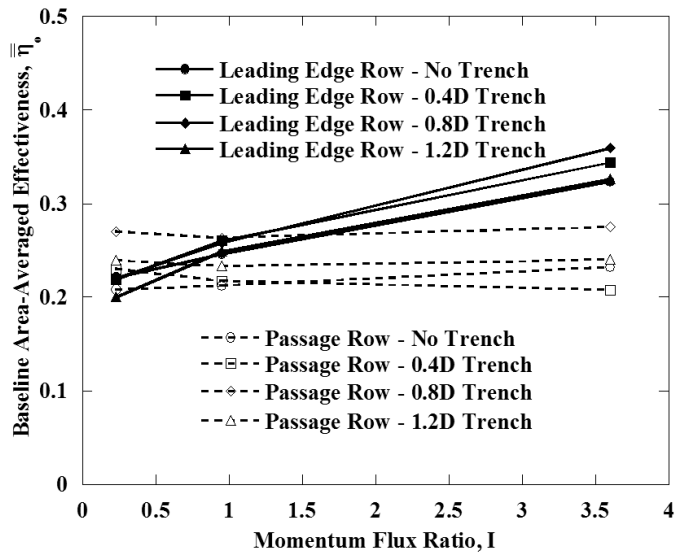


**Figure 5. Baseline area-averaged effectiveness for the leading edge and passage cooling rows with different trench depths and no deposition.**

depth; therefore, deposition simulation and adiabatic effectiveness experiments were conducted with trench depths of 0.4D, 0.8D, and 1.2D. Figure 4 shows adiabatic effectiveness contours before deposition at momentum flux ratios of 0.23 and 3.6 for all trench depths tested in the current study compared with the case with no trench by Lawson and Thole [1]. The contours show that the trenches improve cooling effectiveness between holes for both the leading edge and passage cooling rows. As trench depth increases, cooling effectiveness within the trench improves; however, cooling effectiveness downstream of the trench diminishes. Because of these opposing trends, the medium trench depth of 0.8D provides improved cooling effectiveness within the trench while maintaining adequate cooling downstream of the trench.

The area-averaged effectiveness for the leading edge and passage cooling rows for all trench depths with no deposition are given in Figure 5. The white and black boxed regions shown in Figure 4a represent the areas used for calculating the area-averaged effectiveness for the leading edge and passage cooling rows, respectively. Trench depth had little effect on the leading edge row effectiveness; however, the 0.8D trench yielded the highest area-averaged effectiveness for the passage cooling row. The distinction between trench depths is most obvious at high momentum flux ratios because the trench improves effectiveness by mitigating separation effects that occur at high momentum flux ratios. The trenches allow for increased coolant mass to be supplied without the risk of separation effects. The result is improved cooling between cooling holes and downstream of cooling rows with the trench.

### **Effects of Trench Depth with Deposition**

Deposition simulations were conducted to determine the effects of deposition on cooling effectiveness for all three trench depths. These simulations were carried out at TSP = 1.2 for all cooling conditions at each trench depth. Figure 6 shows photographs of the surface and corresponding adiabatic

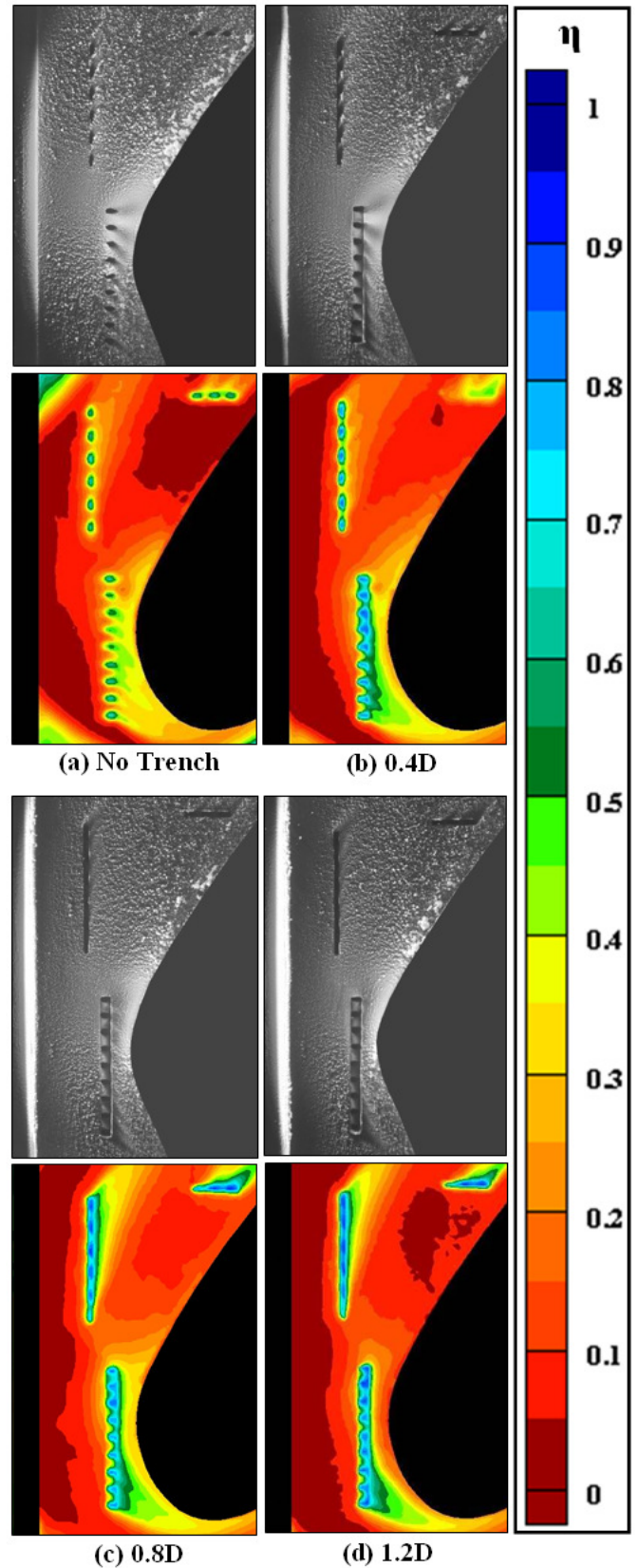


**Figure 6. Surface photos and effectiveness contours at I=3.6 for all trench depths after deposition.**

effectiveness contours after deposition simulation at  $I = 3.6$ . For each case, deposition was most dense in the stagnation region collecting in mounds as deep as  $2D$ . It is important to note that the deposition in the photographs in Figures 6, 11, and 12 is most dense in regions where the deposits are brightest. Lawson and Thole [1] concluded that deposition in the stagnation region was caused by the leading edge vortex. The static pressure gradient through the boundary layer at the stagnation region pulls the flow toward the wall forming a recirculation region. Particles with high inertia become entrained in the leading edge vortex and deposit on the endwall. Figure 6 shows that deposition patterns are highly dependent on trench depth. For the case with no trench, a dense number of deposits collected upstream and between the leading edge cooling holes. The mounds of deposition that collected upstream of the leading edge cooling row in Figure 6a were on approximately  $1D$  in height. Deposition was prevented downstream of that cooling row in areas with good coolant coverage. Figures 6b through 6d show that deposition between the leading edge cooling holes decreased with an increase in trench depth. Downstream of the leading edge cooling row, deposition patterns change noticeably with trench depth. For the  $0.4D$  trench, the downstream deposition pattern looks very similar to the case with no trench. In these cases deposition surrounds the areas where coolant jets divert particle trajectories. For the  $1.2D$  trench, deposition in the stagnation region extends upstream almost to the trailing edge lip of the trench with little to no effect of the coolant jets on deposition. The  $0.8D$  trench, on the other hand, prevents deposition downstream of the trench. The difference in deposition patterns between the  $0.8D$  and  $1.2D$  trenches exists because coolant coverage downstream of the  $0.8D$  trench is uniform with resulting minimum deposition in the stagnation region.

The area-averaged effectiveness resulting from the deposition as well as the percentage reduction of effectiveness for the leading edge cooling row at all trench depths are shown in Figure 7. Note that the percentage values are relative to that same trench geometry with no deposition. All three cases with trenches clearly outperformed the case with no trench. Deposition of particles reduced the leading edge effectiveness by as much as 30% with no trench while the highest reduction for any of the trenced cases was 13%. Area-averaged effectiveness after deposition was highest through the entire range of momentum flux ratios for the case with the  $0.8D$  trench. The cases with the  $0.8D$  trench also yielded the lowest effectiveness reduction out of the three trench depths tested.

In the case with no trench for the passage row of film-cooling holes, there was a dense deposition of particles that collected downstream of the row. As the trench depth increased, the deposition that collected in and around the trench decreased. Effectiveness contours in Figure 6 show that the  $0.8D$  and  $1.2D$  trenches allow for coolant to fill in between cooling holes creating a layer of cool air in the trench. The cool air layer prevents deposition from forming on the trailing edge lip of the trench for the  $0.8D$  and  $1.2D$  trench cases. For the case with no trench and the  $0.4D$  trench, effectiveness contours show minimum cooling between and downstream of holes. The result is deposition collection on the trailing edge lip of the  $0.4D$  trench between cooling holes.

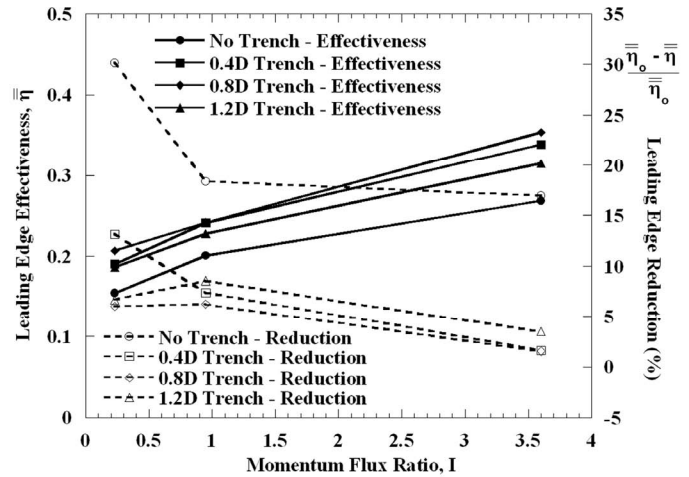


Figure 7. Area-averaged effectiveness and effectiveness reduction for the leading edge row after deposition.

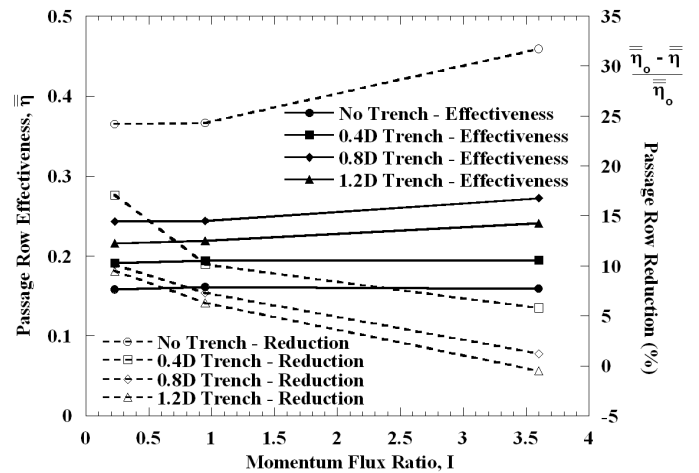


Figure 8. Area-averaged effectiveness and effectiveness reduction for the passage row after deposition.

Figure 8 shows the area-averaged effectiveness after deposition and percentage reduction in effectiveness caused by deposition for the passage cooling row at all trench depths. Results indicate the passage row effectiveness is more sensitive to trench depth than the leading edge row, likely because of the strong influence of the horseshoe vortex at the leading edge. Similar to the leading edge row, the  $0.8D$  trench for the passage row provides better cooling than the other trench depths. The percentage reduction in effectiveness for the case with no trench was as high as 32% while the percentage reduction with the trench was at most 17%. It is interesting to note that the reduction in effectiveness was near zero for the high momentum flux ratio cases at both the leading edge and passage cooling rows. The lack of any effect of deposition for the high momentum flux case is discussed further in the following section.

To quantify the combined cooling effectiveness of the leading edge and passage cooling rows, a total area-average of the two cooling rows was calculated for each case. The total area-average was calculated by taking a weighted area-average of the two representative areas, shown in Figure 4a, using their respective area-averaged values. Figure 9 shows the total area-average values for the cases with no trench and the  $0.8D$  trench

before and after deposition for all three momentum flux ratios tested. The results show that the 0.8D trench is much less sensitive to deposition than the case with no trench. Note that even with deposition, the 0.8D trench performs better than the baseline with no trench and no deposition.

Figure 10 shows photographs of particle trajectories in the stagnation plane for  $I = 0.23$  and  $I = 3.6$  at  $TSP = 1.2$  for no trench and the 0.8D trench. Recall that the image plane is in line with the flow through the centerline of a film cooling hole at stagnation as illustrated in Figure 2. Lines added below each photo in Figure 10 illustrate the film cooling hole location in each image. The images in Figure 10 are composite photographs taken over a time period of approximately 0.01s (20 frames). A range of representative frames were specifically chosen to compose each image to illustrate the dominant flow structures for each cooling condition. Although this method of composing images may be biased toward large particle motion, it is the large particles that contribute most to the deposition. It is important to note that particles are generally moving from left to right and tend to be pulled toward the endwall by the leading edge vortex. The high speed photographs complement the assertion by Lawson and Thole [1] that deposition builds in the endwall corner.

For all cases in Figure 10, particles entrained in the leading edge vortex are pulled toward the endwall downstream of the leading edge cooling row. Figure 10 indicates the leading edge vortex is larger at  $I = 0.23$  than at  $I = 3.6$ . At  $I = 3.6$  the leading edge vortex at stagnation is paired with a secondary vortex that forms upstream of the cooling row. This secondary vortex forms because the coolant jets at  $I = 3.6$  create a blockage effect that causes the flow to wrap toward the endwall upstream of the jets. For the case with no trench, this upstream vortex results in dense deposition between and upstream of cooling holes. The upstream vortex forms farther downstream with the trench than without the trench pulling particles into the trench. Particles that are pulled into the trench either deposit within the trench or are solidified and ejected by the coolant. At  $I = 0.23$  the leading edge vortex is larger with the trench than without

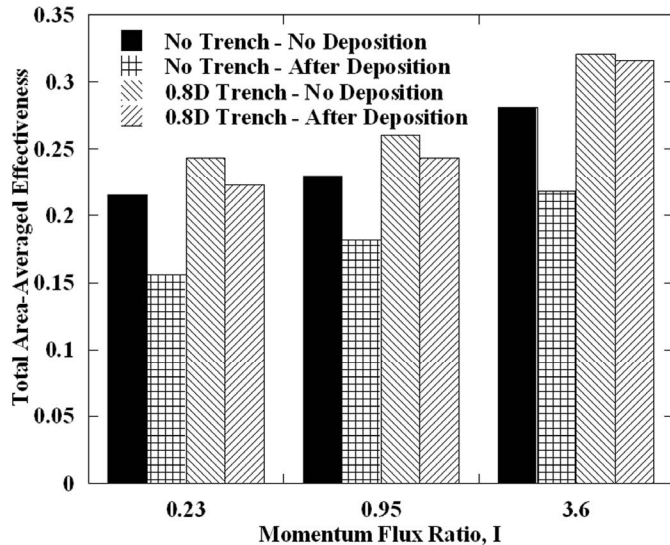


Figure 9. Area-averaged effectiveness of passage and leading edge cooling rows for no trench and the 0.8D trench before and after deposition.

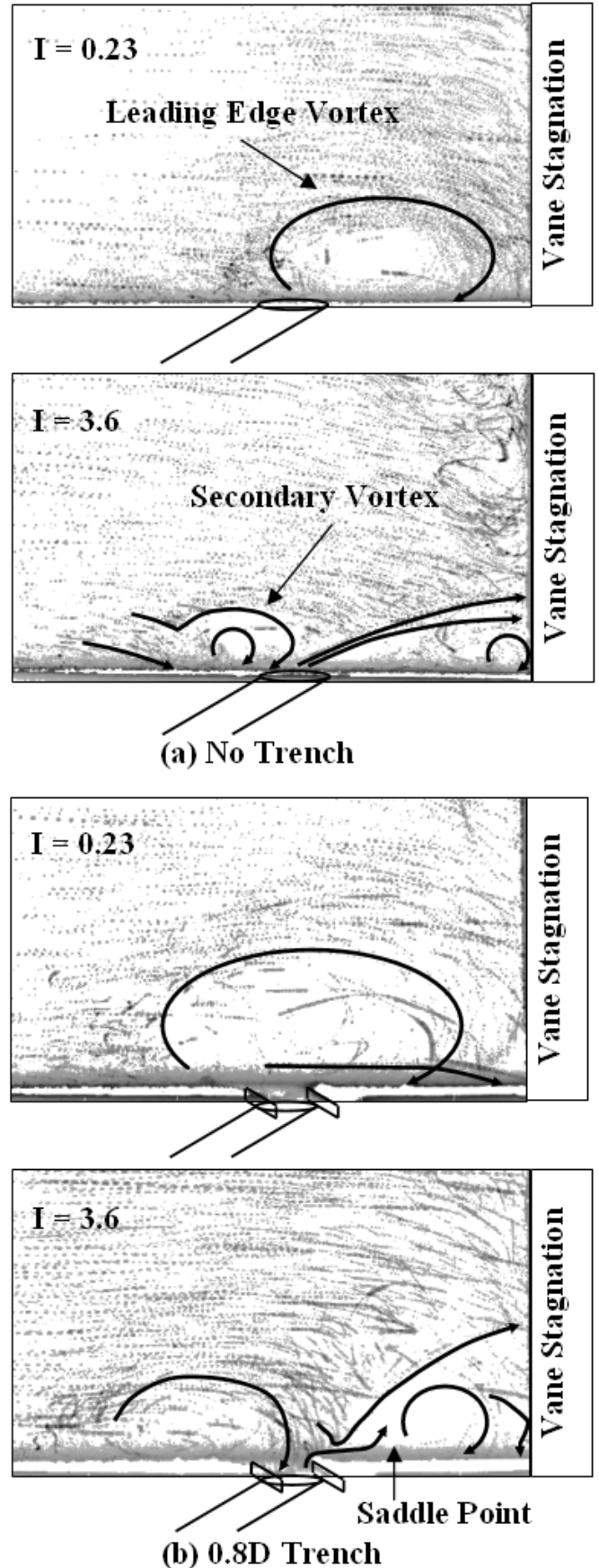


Figure 10. Flow visualization pictures at  $I = 0.23$  and  $I = 3.6$  for (a) no trench and (b) the 0.8D trench.

the trench. Particles entrained in the larger vortex above the trench have less inertia and are more likely to follow fluid streamlines thus preventing deposition. In contrast, particles entrained in the leading edge vortex with no trench have high inertia and are more likely to exit the vortex and deposit on the endwall.

### Effects of Momentum Flux Ratio

Thole et al. [26] showed that momentum flux ratio is a parameter that determines the separation tendency of a film cooling jet. At low momentum flux ratios, coolant jets remain attached to the surface and provide good coolant coverage while at high momentum flux ratios, coolant jets separate leaving the surface exposed to hot mainstream gases. For the case with no trench in Figure 4a, coolant from the leading edge row is pulled toward the suction side of the vane at  $I = 0.23$  providing little coolant coverage along the pressure side. At  $I = 3.6$  coolant separates but is brought back to wash the surface as a result of the spanwise pressure gradient along the vane stagnation thereby providing good coolant coverage near stagnation.

The cooling trend is slightly different for the case with the 0.8D trench as shown in Figure 4c. At  $I = 0.23$  coolant is channeled along the trench toward the suction side of the vane and exits the trench along the suction side of the airfoil. At  $I = 3.6$  coolant also fills the trench but exits along the entire trench width. The additional spreading of the coolant in the trench before exiting to interact with the horseshoe vortex provides better cooling.

Figure 11 shows surface photographs and adiabatic effectiveness contours at all three momentum flux ratios for the 0.8D trench with deposition. All three experiments in Figure 11 were conducted with  $TSP_{max} = 1.2$ . Clear comparisons of deposition photographs and effectiveness contours illustrate that coolant locations correlate with deposition patterns. Deposition is prevented in regions of high cooling for two reasons. First, the jet momentum carries the particles away from the surface. Second, when entrained in coolant gases, particles fully solidify making deposition less likely in the event of surface impaction.

Another interesting trend illustrated in Figure 11 is that deposition between cooling holes in the leading edge trench increases with an increase in momentum flux ratio. This trend can be explained by observing the particle behavior at low and high momentum flux ratios for the 0.8D trench in Figure 10b. At  $I = 0.23$ , the leading edge vortex near stagnation pulls particles toward the endwall to deposit downstream of the cooling row. At  $I = 3.6$  two vortices are present: one upstream, and the other downstream of the film-cooling holes. The upstream vortex pulls particles toward the endwall creating a mechanism for high inertia particles to be carried into the trench to deposit. Even though particles are pulled into the trench at high momentum flux ratios, the amount of coolant in the trench reduces deposition as compared to the case with no trench. As illustrated in Figure 6a, little coolant coverage between cooling holes results in large amounts of deposition with no trench.

In general, the 0.8D trench mitigates the negative effects of deposition on cooling effectiveness particularly at high

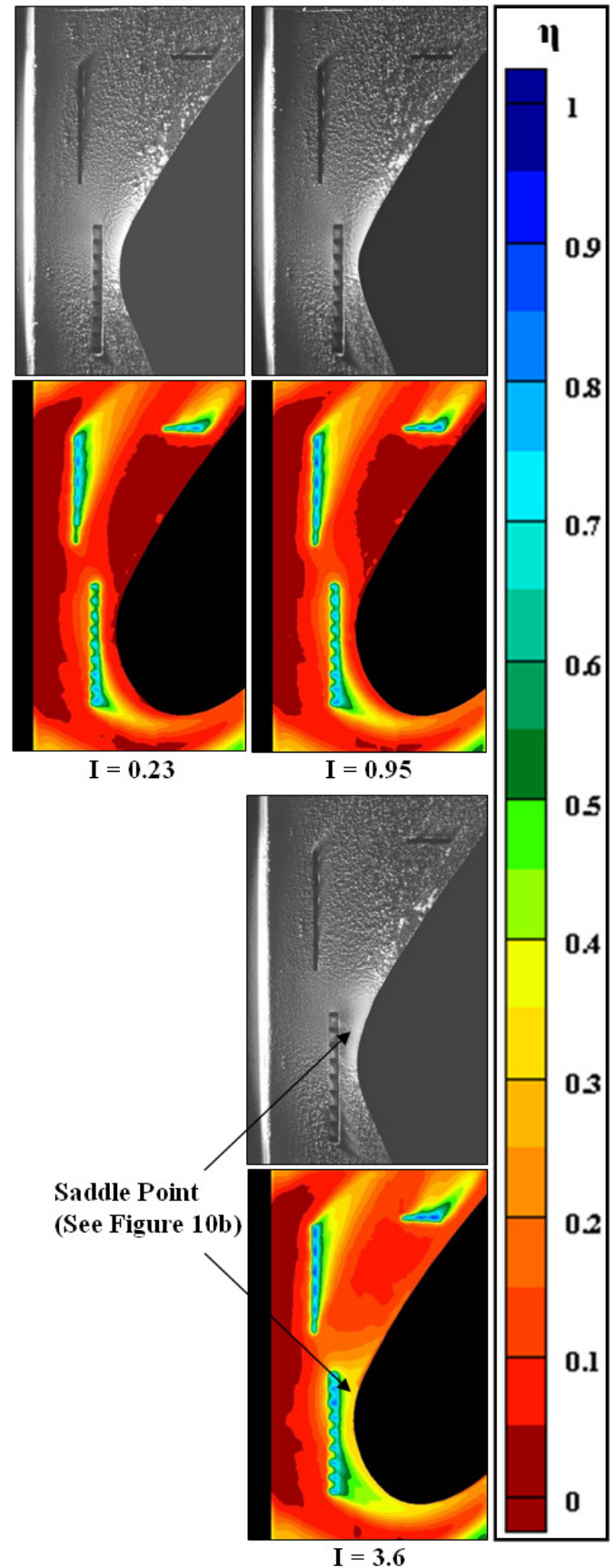


Figure 11. Surface photos and effectiveness contours for the 0.8D trench at all momentum flux ratios after deposition at  $TSP_{max} = 1.2$ .

momentum flux ratios. Coolant coverage improves with an increase in blowing ratio which leads to a decrease in deposition coverage. As the extent of deposition decreases, the effect that it has on cooling effectiveness also decreases. In addition, the trench reduces deposition between cooling holes by creating a pocket of coolant along the length of the cooling row that acts as a protective barrier against deposition.

### Effects of Thermal Scaling Parameter

For results presented in the previous sections, deposition was simulated with  $TSP_{max} = 1.2$  for which most particles were solid and only the largest particles were molten. Additional experiments were conducted with  $TSP_{max} = 2.2$  to determine the effects of particle phase on cooling effectiveness for the 0.8D trench. At  $TSP_{max} = 2.2$ , particles smaller than  $70\mu m$  were in solid form and particles larger than  $70\mu m$  were in molten form upon reaching the test section.

Figure 12 shows deposition photographs and cooling effectiveness contours at  $I = 0.23$  and  $3.6$  for  $TSP_{max} = 1.2$  and  $2.2$ . The differences between the two  $TSP_{max}$  values are small. At  $I = 0.23$  deposition collected farther downstream on both the suction and pressure sides of the vane at  $TSP_{max} = 2.2$  than at  $TSP_{max} = 1.2$ . Deposition collected more densely downstream of the passage row at  $TSP_{max} = 2.2$  than at  $TSP_{max} = 1.2$ . These differences exist because particles at  $TSP_{max} = 2.2$  are softer and stickier than at  $TSP_{max} = 1.2$ .

The photographs in Figure 12b show that deposition downstream of the leading edge row was again very similar between the two  $TSP_{max}$  values. Dense deposition extended farther downstream on the pressure side at  $TSP_{max} = 2.2$  than at  $TSP_{max} = 1.2$ ; however suction side deposition looks identical between the two  $TSP_{max}$  cases. Downstream of the leading edge row near stagnation the deposition pattern between the two  $TSP_{max}$  cases appears slightly different. At  $TSP_{max} = 2.2$  deposition filled in between cooling jets making individual jets more visible than at  $TSP_{max} = 1.2$ . Downstream of the leading edge row coolant spreading was better at  $TSP_{max} = 2.2$  than at  $TSP_{max} = 1.2$  because of reduced deposition in the stagnation region at  $TSP_{max} = 2.2$ . Lawson and Thole [1] found that deposition near stagnation decreased with increasing  $TSP_{max}$  because particles entrained in the leading edge vortex were more likely to deposit on the vane surface than on the endwall when they were soft and sticky.

Effectiveness reduction compared with the baseline cases without deposition for the leading edge and passage cooling rows at both  $TSP_{max}$  values is shown in Figure 13. At low momentum flux ratios, effectiveness reduction is slightly higher at  $TSP_{max} = 2.2$  than at  $TSP_{max} = 1.2$ , while at  $I = 3.6$ , differences in effectiveness reduction between the two  $TSP_{max}$  cases is almost negligible. The negative effectiveness reduction at  $I = 3.6$  and  $TSP_{max} = 2.2$  for the leading edge row suggests a slight improvement in effectiveness caused by deposition; however, the improvement is small ( $<3\%$ ). The small differences in effectiveness reduction between the two  $TSP_{max}$  cases, indicates that the 0.8D trench mitigates the negative effects of deposition regardless of particle phase particularly at high momentum flux ratios.

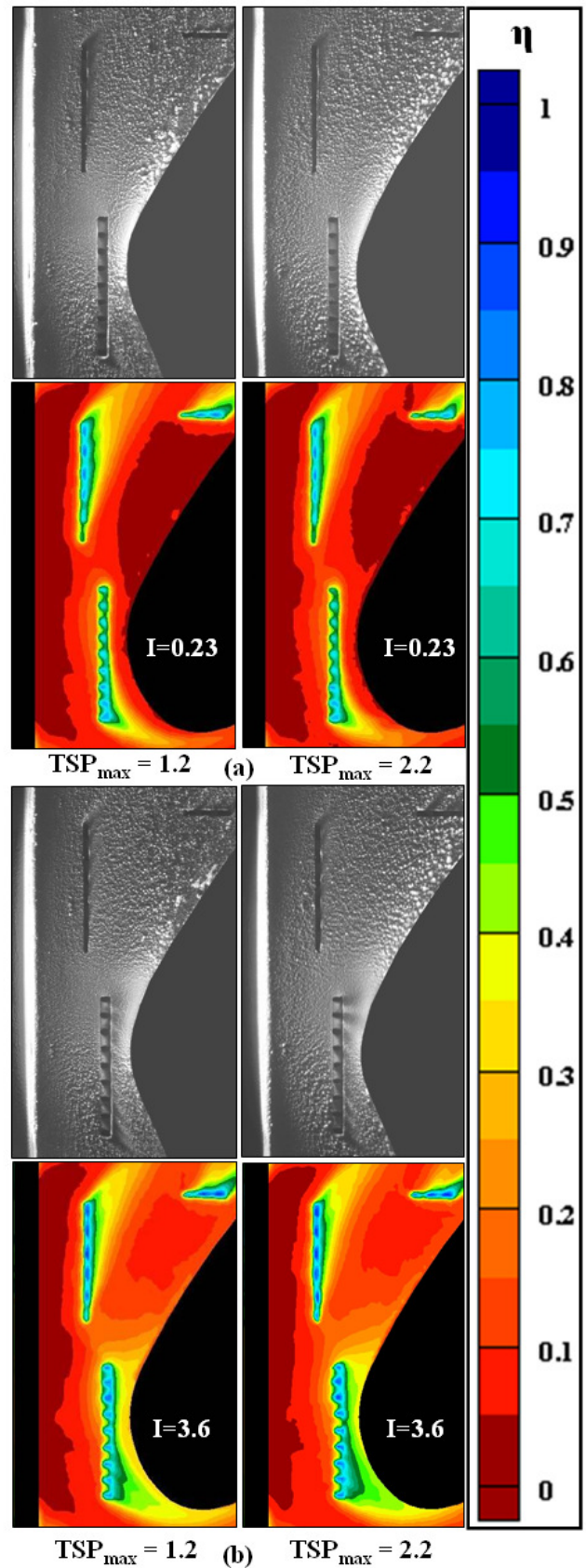


Figure 12. Surface photographs and adiabatic effectiveness contours after deposition for the 0.8D trench at (a)  $I = 0.23$  and (b)  $I = 3.6$ .

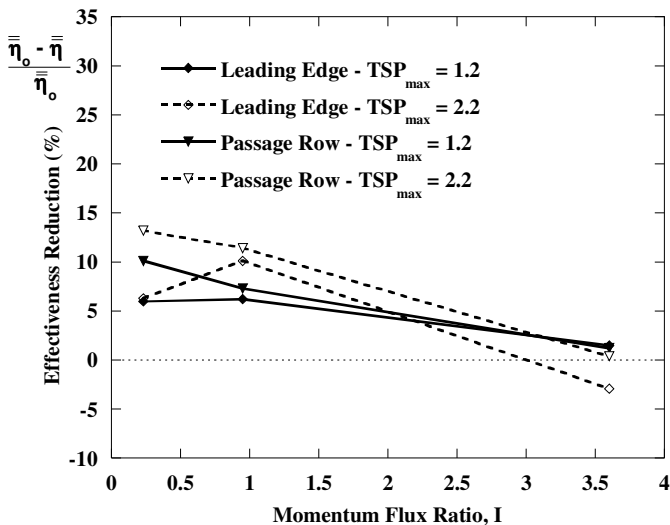


Figure 13. Effectiveness reduction for the leading edge and passage rows for the 0.8D trench at  $TSP_{max} = 1.2$  and  $TSP_{max} = 2.2$ .

## CONCLUSIONS

Particle deposition was simulated dynamically using wax in a large scale vane cascade model with endwall film cooling. Cooling effectiveness was quantified for three narrow, transverse trench film-cooling geometries before and after deposition. The effects of trench depth, momentum flux ratio, and thermal scaling parameter on adiabatic effectiveness were quantified for the leading edge and passage cooling rows near the vane endwall junction.

Although all three trench geometries tested clearly outperformed the geometry with no trench, results showed that the medium trench depth of 0.8D outperformed all other geometries both before and after deposition for both the leading edge and passage cooling rows. As trench depth increased, cooling effectiveness within the trench increased while effectiveness downstream of the trench decreased.

The effectiveness reduction caused by deposition was similar for all three trench depths but clearly decreased with an increase in momentum flux ratio. For trench film-cooling geometries deposition reduced effectiveness by less than 5% at  $I = 3.6$ .

Deposition within trenches increased with an increase in momentum flux ratio. Flow visualization results from a high speed camera system showed that an upstream vortex formed at high momentum flux ratios pulling particles into the trench; however, deposition within the trench was not as severe as deposition between cooling holes with no trench. The trench creates a pocket of coolant along the entire row of holes that acts as a protective barrier against deposition.

Experiments were conducted at two  $TSP_{max}$  values for the best trench depth of 0.8D revealed that effectiveness reduction was independent of particle phase. The findings from the current study confirm that trench cooling geometries can be used to mitigate the negative effects of particle deposition particularly at high momentum flux ratios. The 0.8D trench depth should be considered for use in the first stage vane row in turbines with traces of impurities in the fuel and air.

## ACKNOWLEDGMENTS

This publication was prepared with the support of the US Department of Energy (DOE), Office of Fossil Fuel, and the National Energy Technology Laboratory (NETL). Any opinions, findings, conclusions, or recommendations expressed herein are solely those of the authors and do not necessarily reflect the views of the DOE. The writers would like to specifically thank Jason Albert and Dr. David Bogard for their continued communication and support on the subject matter. This research was conducted under a subcontract that was sponsored by the U.S. DOE-NETL through a cooperative agreement with the South Carolina Institute for Energy Studies at Clemson University.

## REFERENCES

- [1] Lawson, S.A., and Thole, K.A., 2010, "Simulations of Multi-Phase Particle Deposition on Endwall Film-Cooling," GT2010-22376.
- [2] Harrison, K.L., Dorrington, J.R., Dees, J.E., Bogard, D.G., and Bunker, R.S., 2007, "Turbine Airfoil Net Heat Flux Reduction with Cylindrical Holes Embedded in a Transverse Trench," GT2007-27996.
- [3] Sundaram, N., and Thole, K.A., 2008, "Bump and Trench Modifications to Film-Cooling Holes at the Vane-Endwall Junction," *J. of Turbomachinery*, **130**(4).
- [4] Somawardhana, R.P., and Bogard, D.G., 2007b, "Effects of Obstructions and Surface Roughness on Film Cooling Effectiveness with and without a Transverse Trench," GT2007-28003.
- [5] Bunker, R.S., 2002, "Film-Cooling Effectiveness due to Discrete Holes within a Transverse Surface Slot," GT2002-30178.
- [6] Waye, S.K., and Bogard, D.G., 2006, High Resolution Film Cooling Effectiveness Measurements of Axial Holes Embedded in a Transverse Trench with Various Trench Configurations," GT2006-90226.
- [7] Jensen, J.W., Squire, S.W., Bons, J.P., and Fletcher, T.H., 2005, "Simulated Land-Based Turbine Deposits Generated in an Accelerated Deposition Facility," *J. of Turbomachinery*, **127**, pp. 462-470.
- [8] Smith, C., Barker, B., Clum, C., and Bons, J., 2010, "Deposition in a Turbine Cascade with Combusting Flow," GT2010-22855.
- [9] Wenglarz, R.A., and Fox, R.G., 1990, "Physical Aspects of Deposition From Coal-Water Fuels Under Gas Turbine Conditions," *J. of Engineering for Gas Turbines and Power*, **112**, pp. 9-14.
- [10] Walsh, P.M., Sayre, A.N., Loehden, D.O., Monroe, L.S., Beer, J.M., and Sarofim, A.F., 1990, "Deposition of Bituminous Coal Ash on an Isolated Heat Exchanger Tube: Effects of Coal Properties on Deposit Growth," *Progress in Energy Combustion Science*, **16**, pp. 327-345.
- [11] Richards, G.A., Logan, R.G., Meyer, C.T., and Anderson, R.J., 1992, "Ash Deposition at Coal-Fired Gas Turbine Conditions: Surface and Combustion Temperature Effects," *J. of Energy for Gas Turbines and Power*, **114**, pp. 132-138.
- [12] Wenglarz, R.A., and Wright, I.G., 2003, "Alternate Fuels for Land-Based Turbines," *Proceedings of the Workshop*

on Materials and Practices to Improve Resistance to Fuel Derived Environmental Damage in Land-and Sea-Based Turbines, Oct. 22-24, Co. School of Mines, Golden, Co., pp. 4-45 to 4-64.

- [13] Ai, W., Laycock, R.G., Rappleye, D.S., Fletcher, T.H., and Bons, J.P., 2009, "Effect of Particle Size and Trench Configuration on Deposition from Fine Coal Flyash near Film Cooling Holes," GT2009-59571.
- [14] Lawson, S.A., and Thole, K.A., 2009, "The Effects of Simulated Particle Deposition on Film Cooling," GT2009-59109.
- [15] Albert, J.E., Keefe, K.J., and Bogard, D.G., 2009, "Experimental Simulation of Contaminant Deposition on a Film Cooled Turbine Airfoil Leading Edge," IMECE2009-11582.
- [16] Baines, W.D., and Peterson, E.G., 1951, "An Investigation of Flow Through Screens," *Transactions of ASME*, **73**, pp. 467-480.
- [17] Radomsky, R.W., and Thole, K.A., 2000, "Flowfield Measurements for a Highly Turbulent Flow in a Stator Vane Passage," *J. of Turbomachinery*, **122**, pp. 255-262.
- [18] Moffat, R.J., 1988, "Describing the Uncertainties in Experimental Results," *Exp. Therm. Fluid Sci.*, **1**, pp. 3-17.
- [19] Dring, R.P., Caspar, J.R., and Suo, M., 1979, "Particle Trajectories in Turbine Cascades," *J. of Energy*, **3** (3), pp. 161-166.
- [20] Bons, J.P., Crosby, J., Wammack, J.E., Bentley, B.I., and Fletcher, T.H., 2007, "High Pressure Turbine Deposition in Land-Based Gas Turbines From Various Synfuels," *J. of Turbomachinery*, **129**, pp. 135-143.
- [21] Li, R., Lei, W., Yang, T., and Raninger, B., 2007, "Investigation of MSWI fly ash melting characteristic by DSC-DTA," *Waste Management*, **27**, pp. 1383-1392.
- [22] Krishnaiah, W., and Singh, D.N., 2006, "Determination of thermal properties of some supplementary cementing materials used in cement and concrete," *Construction and Building Materials*, **20**, pp. 193-198.
- [23] Wang, Q., Tian, S., Wang, Q., Huang, Q., and Yang, J., 2008, "Melting characteristics during the vitrification of MSWI fly ash with a pilot-scale diesel oil furnace," *J. of Hazardous Materials*, **160**, pp. 375-381.
- [24] Dennis, R.A., Shelton, W.W., and Le P., 2007, "Development of Baseline Performance Values for Turbines in Existing IGCC Applications," GT2007-28096.
- [25] Johnson, D., 1996, Original Pratt & Whitney contact regarding operating conditions and geometric specifications of PW6000 nozzle guide vane.
- [26] Thole, K.A., Sinha, A.K., and Bogard, D.G., 1990, "Mean Temperature Measurements of Jets with a Crossflow for Gas Turbine Film Cooling Application," *Rotating Transport Phenomena*, Kim, J.H., and Yang, W.J., ed. Hemisphere Publishing Corporation, New York, New York.